Giant Anisotropic Raman Response of Encapsulated Ultrathin Black Phosphorus by Uniaxial Strain

Yanyong Li, Zhixin Hu, Shenghuang Lin, Sin Ki Lai, and Wei Ji, Shu Ping Lau**

Y. Y. Li,[⊥] Dr. S. H. Lin, S. K. Lai, Prof. S. P. Lau

Department of Applied Physics, the Hong Kong Polytechnic University, Hung Hom, Kowloon, Hong Kong, P. R. China

E-mail: apsplau@polyu.edu.hk

Dr. Z. X. Hu,[⊥] Prof. W. Ji

Department of Physics and Beijing Key Laboratory of Optoelectronic Functional Materials & Micro-Nano Devices, Renmin University of China, Beijing 100872, P. R. China

E-mail: wji@ruc.edu.cn

[⊥] *These authors contributed equally.*

Keywords: black phosphorus, uniaxial strain, Raman spectroscopy, Grüneisen parameter, anisotropy

Abstract

We report the giant anisotropic Raman response of encapsulated ultrathin black phosphorus (BP) by uniaxial strain. A modified bending technique is employed to apply precise uniaxial tensile strain along the zigzag or armchair direction of the ultrathin BP encapsulated by a layer of polymethyl methacrylate (PMMA). The Raman shift rates of the A_g^1 , B_{2g} and A_g^2 modes are significantly distinct for strain applied along different directions. For the strain applied along zigzag direction, the Raman shift rate of the B_{2g} mode can reach a remarkable value of ~ -11 cm^{-1}/% strain. In addition, the Grüneisen parameter is as high as ~ 2.5, which is the largest among all the reported common two-dimensional materials. Density functional perturbation theory calculations are performed to understand the exceptional anisotropic strain response discovering that not only the bond lengths but also the bond angels are changed in the strained ultrathin BP, which lead to the giant anisotropic Raman response. Furthermore, we demonstrate an alternative method based entirely on the strained ultrathin BP and non-polarized Raman spectroscopy to determine the crystallographic orientations of ultrathin BP. This work paves a way to study the strain-induced anisotropic electrical conductance and magnetotransport properties of BP.

1. Introduction

The research on two-dimensional (2D) layered materials, such as graphene, molybdenum disulfide (MoS_2) and hexagonal boron nitride has sprung up owing to their outstanding electronic, optical and structural properties.[1-3] Black phosphorus (BP), the most stable allotrope of phosphorus, has joined into the 2D materials family recently. It also has a layered structure like graphite. Analogously, BP can be exfoliated down to atomically thin from bulk crystal like its counterparts. In contrast to the zero band gap graphene, BP has a thickness-dependent band gap varying from 0.3 eV (bulk) to 2.0 eV (monolayer).[4-6] Notably, unlike the perfectly flat layer in graphene, colossal anisotropy in ultrathin BP can be observed due to its puckered honeycomb structure, which results in lots of intriguing features. For example, it has been reported that electrical conductance along the armchair (AC) direction is about 1.5 times larger than that along the zigzag (ZZ) direction.[7] On the other hand, the ZZ direction is a preferential thermal conduction path in ultrathin BP, which is about twice as high as that along AC orientation.[8] In addition, a number of theoretical calculations have predicted that the anisotropic electrical and thermal properties of ultrathin BP can be modified by strain engineering [9, 10] or vertical external electric fields [11]. Obviously, strain engineering is a more direct and convenient way to modulate the lattice structure so as to influence the phonon dispersion[12] and electron band structure[13], particularly in 2D materials, because they are highly flexible and easier to be strained.[14-16] Recently, it is predicted that monolayer BP can sustain a remarkable tensile strain of 30%.[17] Together with the inherent anisotropic properties, ultrathin BP could pave the way for creating novel strain tunable devices. However, experimental demonstration of the anisotropic strain response in ultrathin BP is still lacking presumably due to the instability of ultrathin BP in ambient air which may degrade within hours.[18-20] Wang *et al.* used a bending technique to apply tensile strain to ultrathin BP without proper encapsulation, the Raman shift rates of the three characteristic Raman modes (A_g^1 , B_{2g} and A_g^2) in the ultrathin BP were not exceptionally large.[21] Herein, we demonstrate a modified bending technique which could supply a precise anisotropic uniaxial strain to an ultrathin BP encapsulated by a layer of PMMA. Remarkably, the three Raman modes not only show

extraordinary large Raman shift rates but also exhibit distinctive anisotropic strain responses. For the strain applied along ZZ direction, the Raman shift rate of the B_{2g} mode is the largest among the three Raman modes and is approaching ~ -11 cm^{-1}/% which is about 5 times larger than the recently reported value.[21] Combining the density-functional perturbation theory (DFT) calculation results, we experimentally derive the in-plane Grüneisen parameter of the B_{2g} mode to be 2.47, which is the largest among all the known values of common 2D materials such as grapheme and MoS_2. Furthermore, the extremely high anisotropic strain sensitivity of B_{2g} mode can be utilized to identify the crystallographic orientations of ultrathin BP. We reveal that without the aid of polarized Raman spectroscopy, the AC and ZZ directions of the ultrathin BP can also be determined by monitoring the variation of Raman shift of the B_{2g} mode in strained BP. Compared with other methods,[7, 22-24] our method is simple and convenient to determine the crystallographic orientations of ultrathin BP without complicated setup and especially useful for ultrathin BP on flexible substrates.

2. Results and Discussion

BP has an orthorhombic lattice (D_{2h}^{18} point group)[25] where each phosphorus atom is covalently bonded to three neighboring atoms as shown in **Figure 1**a. Due to the sp^3 hybridization, the phosphorus atoms in an atomic layer are not coplanar which results in the appearance of ridge and accordion structure. Figure 1b shows a typical high-resolution transmission electron microscopy image of the mechanically exfoliated BP. The high crystallinity of the BP can be observed. Analogous hexagonal atomic arrangement is obviously found from the contrast of the image, which is displayed by red balls in Figure 1b. The lattice plane spacing is measured to be 0.217 nm ascribed to the (002) lattice planes by comparing with ICDD-PDF: No.76-1963. Figure 1c illustrates the schematic diagram of the experimental setup and the inset is the cross-sectional view of the encapsulated ultrathin BP. Through bending the flexible polyethylene terephthalate (PET) substrate, the induced strain (ε) can be calculated based on the formula,[26] $\varepsilon = d / 2r$, where d is the thickness of the substrate and r is the radius of curvature of the bended substrate as shown in the inset of Figure 1c.

The photo of the experimental set up showing the bended substrate is shown in **Figure S1** (Supporting Information). Figure 1d shows a typical Raman spectrum of the encapsulated ultrathin BP on the PET substrate without externally applied strain. The three characteristic Raman modes, A_g^1 , B_{2g} and A_g^2 , are revealed approximately at 363 cm^{-1}, 441 cm^{-1} and 468 cm^{-1} respectively, which are in good agreement with the literature.[27, 28] The inset of Figure 1d illustrates the atomic displacements giving rise to the three characteristic modes.

Atomic force microscopy (AFM) was employed to determine the thickness of the BP after the completion of all the measurements and washed away the encapsulated PMMA layer as shown in **Figure 2**a. The bottom inset in Figure 2a depicts that the BP flake has a thickness of 7.75 nm corresponding to ~15 layers.[29] Unless otherwise stated, Raman spectroscopy measurements are based on this sample here. Angle-resolved polarized Raman spectroscopy was used to identify the ZZ and AC orientations of the BP at first.[22] According to the Raman selection rule, Raman intensity depends on the vibrational symmetry of the scattering system, which reaches local maxima (minima) when the incident laser polarization direction is parallel (perpendicular) to the corresponding atomic displacement.[30] In our experiment, the polarization direction of the incident laser with respect to the sample orientation is defined as θ, which is tuned arbitrarily by a half-wave plate as shown in the top inset of **Figure 2**a. The direction of the analyzer is parallel to the initial polarization direction of the incident laser. It is observed that the Raman intensities of the three characteristic modes exhibit strong dependence on the polarization angles θ as shown in **Figure 2**b. The two A_g modes almost disappear at $\theta = 0°$ and arrive at their vertices at $\theta = 90°$, while the B_{2g} mode shows an opposite trend. The variations of the Raman mode intensities are in agreement with sinusoidal functions,[31]

$$I(A_g) = [\frac{a-c}{2}\cos(2\varphi - \theta) + (\frac{a+c}{2})\cos\theta]^2 \quad (1)$$

$$I(B_{2g}) = e^2[cos(2\varphi + \theta)]^2 \quad (2)$$

where *a*, *c*, and *e* are the corresponding parameters in Raman tensors of A_g and B_{2g} modes and φ is the direction of ZZ orientation corresponding to sample configuration. Detailed explanation can be found in Supporting Information. Therefore, we utilized **Equations (1)** and **(2)** to fit the obtained experimental data and found that the experimental results are in good agreement with the fitted lines as shown in Figure 2c,d respectively. Combing the effect of sample thickness and excitation laser wavelength,[32, 33] the A_g^2 mode reaches its local maxima at about 90° indicating that θ = 90° is the AC orientation in this ultrathin BP flake.

In reference to the two obtained characteristic orientations, uniaxial strain is applied along the ZZ and AC directions to investigate the evolution of Raman spectroscopy in a non-polarized configuration. As the strain applied along ZZ direction is increased gradually, the red shifts of the B_{2g} and A_g^2 modes are observed while the A_g^1 mode remains unchanged as shown in **Figure 3**a. When the strain is turned orthogonally along the AC direction, the outcomes are significantly different from the former. As shown in **Figure** 3b the A_g^2 mode remains unchanged as the strain increases, while the other two modes show apparent red shifts. Unlike the doubly degenerate Raman modes in graphene and MoS_2,[26, 34-36] there are no obvious peak splitting for these three Raman modes in both cases. **Figure 3**c shows the peak positions of the A_g^1, B_{2g} and A_g^2 modes fitted by Lorentz function under strain along the ZZ and AC directions. It is found that increasing strain causes the Raman modes to soften gradually, implying that the energy of the corresponding phonon modes declines and thus weakens the associated restoring force in these vibrations. In addition, the full-width-at-half-maximum of the three Raman modes as a function of the applied strain is shown in **Figure S3** (Supporting Information). In general, the A_g^2 mode broadens as the strain increases regardless of the directions of the applied strain. **Table 1** presents the anisotropic Raman shift rates of the three modes obtained by linear fitting. The Raman shift rates ($\partial\omega/\partial\varepsilon$) of A_g^2 and B_{2g} modes are much larger than that of A_g^1 mode under the ZZ strain. Specifically, the Raman shift rate of the B_{2g} mode is about

-11 cm^{-1}/% which is much larger than the in-plane Raman mode in MoS_2.[26, 37, 38] Furthermore, it is found that the B_{2g} mode is much more sensitive to the ZZ strain than the A_g^2 mode which is attributed to the fact that the atomic displacement in the B_{2g} mode is mainly along the ZZ orientation. As for the AC case, the Raman shift rates of B_{2g} and A_g^2 modes are dropped greatly except the A_g^1 mode as revealed in **Table 1**. It demonstrates that the effect of strain along the AC direction is moderated on these two in-plane Raman modes. Particularly, the A_g^2 mode almost maintains its original peak position as the strain increases gradually. It may be attributed to the different stiffness in the ultrathin BP along different orientations. The bonding force along the AC direction is weaker than that along the ZZ direction so that it is softer along the AC orientation.[12, 39] The similar strain anisotropy trends can also be found in thicker samples (9.68, 11.2 and 42.9 nm) as shown in **Figure S4** (Supporting Information). But generally, the Raman shift rates of the three modes reduce as the thickness of the BP increases.

The vibrational properties based on a 4L-BP model (4-layer BP) were calculated by using the DFT method to understand the giant strain anisotropy in ultrathin BP. Although the thickness is smaller than the real experiment, it has been proved that the differences in frequencies between 4L-BP and bulk BP for those three optical modes are smaller than 1 cm^{-1} in a previous calculation.[40] The simulated variation trends of the three optical modes are shown by dash dot lines in **Figure 3**c, which are fitting the experimental results quite well under both ZZ and AC strain. The analysis of molecular structure under uniaxial tensile strain allows us to investigate the origin of exceptional strain anisotropy of ultrathin BP. A research of the structural deformation under uniaxial strain has been performed very recently, however, the work has focused on the changes of bond lengths only.[21] We emphasize that the bond angles are also changed under uniaxial strain, which accounts for the giant anisotropic strain response in vibrational modes. Five relevant structural parameters are considered including three P-P distances (R_1, R_2 and R_3) and two angles (θ_1 and θ_2) as shown in **Figure 3**d. The maximum strain is increased to 1.5% in order to minimize the numerical errors. Our results are not

fully consistent with the bond lengths in the previous work,[21] which is most likely attributed to a different choice of Poisson's ratio. As shown in the inset of **Figure 1**d, the A_g^1 mode corresponds to atomic vibration mostly along the out-of-plane direction as well as a small proportion along the in-plane direction. The A_g^2 mode is orthogonal to the A_g^1 mode. The B_{2g} mode is totally along the in-plane direction. They have different dependence on the structural parameters. In the ZZ case, **Figure 3**e shows that the strain stretches R_1 and enlarges θ_1 obviously. A strain of 1.5% increases R_1 by 0.015 Å and θ_1 by 1.04°, while the changes of R_2, R_3 and θ_2 are much smaller. The slope of R_1 under the ZZ uniaxial strain is 0.01 Å/% strain as listed in **Table 2**, which is much larger than that in the AC case. Similar huge difference can also be found for the variation of θ_1. The drastic changes of R_1 and θ_1 extends the *y*-axis separation of atoms in each sublayer lowering the restoring force along *x* and *y*, which results in the giant red-shifts of B_{2g} and A_g^2 modes. The vibration of the A_g^1 mode is basically along the out-of-plane direction, hence it is not affected by changing R_1 and θ_1. By comparison, there are apparent increases of θ_2 and R_3 under the AC uniaxial strain as well as a slightly stretched R_1. The greatly increased θ_2 with a slope of 0.353°/% strain creates a shear-like motion between the two nearby sublayers. The out-of-plane restoring force between the two sublayers is weakened while the in-plane one is strengthened, which softens the A_g^1 mode and enhances the A_g^2 mode. Simultaneously, the slightly stretched R_1 softens A_g^2 and B_{2g}. As a result, we found the red-shifted A_g^1 and B_{2g} as well as the almost unchanged A_g^2 in the AC case. Additionally, the value of R_3 represents the strength of the interlayer interaction, which has very limited effect on the frequency shifts of the optical modes because its intensity is so small that the interlayer restoring forces are much smaller than intralayer ones for both the in-plane and out-of-plane directions.[40] Therefore, the effect of the changing R_3 can be ruled out in both cases.

Grüneisen parameter (γ) represents the rate of phonon frequency changes with respect to strain according to the principle of anharmonicity of the interatomic potentials of the atoms, which can be calculated with a simple formula as follows, [36, 41]

$$\gamma = -\frac{1}{\omega^0(1-\nu)}\frac{\partial\omega}{\partial\varepsilon} \quad (3)$$

where ω^0 and ω are the Raman frequencies at the zero strain and a finite strain, respectively. ε is the uniaxial strain applied to the ultrathin BP, which is composed of the longitudinal (ε_{long}) and the transverse (ε_{tran}) components. The ε_{long} is along the applied strain direction, while the ε_{tran} is perpendicular, which can be expressed as $\varepsilon_{long} = \varepsilon$ and $\varepsilon_{tran} = -\nu\varepsilon_{long}$ where ν is the Poisson's ratio.[38] For the case of uniaxial strain, it is difficult to calculate the Grüneisen parameters separately for the three optical phonon modes because of the lack of the knowledge of the ν value for suspended ultrathin BP, which depends on whether good adhesion exists between the ultrathin BP and the substrate.[42] In fact, no outliers have been observed in the whole process of measurement and the results are highly reproducible. For each applied strain level, the measurement was performed at least 4 times to form the error bars of the data points presented in **Figure 3**c, it demonstrates that neither obvious slipping nor corrugation of the ultrathin BP sample occurs during the experiment. Moreover, the small hysteresis of the Raman shift of the B_{2g} mode between loading and unloading strain further demonstrates that the slipping in our experiment is negligible as shown in **Figure S5** (Supporting Information). The ultrathin BP was deposited onto a ~0.121 mm thick PET substrate covered with a layer of SU-8 film. The SU-8 is a transversely isotropic material with ν of 0.33 which has been used to calculate Grüneisen parameters of graphene and MoS_2.[36, 38] Therefore, based on **Equation (3)** with ν = 0.33, we can obtain the Grüneisen parameters of the ultrathin BP under applied strain along ZZ (θ = 0°) and AC (θ = 90°) directions as listed in **Table 1**. The Grüneisen parameters of these modes are remarkably distinct when strain is applied along different directions, which is further indicating the intrinsic strong anisotropy of phononic properties of ultrathin BP. The in-plane

Grüneisen parameter of the BP (7.75 nm thick) can reach 3.69 ($\gamma_{B_{2g}}$), which is nearly twice the value to that of graphene ($\gamma_G = 1.99$)[29] and over six-times to that of MoS_2 ($\gamma_{E^1_{2g}} = 0.6$)[37] implying that an extraordinary anharmonic effect and strong phonon-phonon interaction in ultrathin BP. **Table S1** (Supporting Information) lists out the values of in-plane Grüneisen parameter of graphene and MoS_2 in the literature. The in-plane Grüneisen parameter of our BP is exceptionally large, despite the relatively thick BP was measured here as compared with the usually monolayer counterparts. However, the measured Grüneisen parameters for other 2D materials are not very consistent among different groups due to the issue of ν as shown in Table S1 (Supporting Information).[42] As already discussed in this work, there is no obvious slipping between the ultrathin BP sample and SU-8 film in our highly reproducible experiment. Thus, we calculated the Grüneisen parameters of BP with a 4L-model under uniaxial strain by the DFT method using $\nu = 0$ and $\nu = 0.33$, which represent whether there is in-plane deformation of the SU-8 film along the direction transverse to the applied strain direction. The calculated Grüneisen parameters with different ν values under ZZ and AC strain are also listed in **Table 1**. In terms of the ZZ direction, the theoretical Grüneisen parameters with ν =0 are qualitatively similar to those with ν = 0.33 and these values are highly comparable with the associated experimental values, especially for the B_{2g} and A_g^2 modes which have larger Raman shift rates. However, in the AC case, the A_g^1 and B_{2g} modes are shortened under strain but the A_g^2 mode is nearly unchanged. By comparing with the calculated Raman shfit rates with different ν values, the results with ν = 0 give a better matched values. On the contrary, ν = 0.33 gives the largely increased values in B_{2g} and A_g^2 modes, which is obviously inconsistent with the experiments. The error for the calculated frequencies in our simulation is estimated as 0.4 cm^{-1} for the maxima, which means 1.6 $cm^{-1}/\%$ strain for the Raman shift rate and 0.4 for Grüneisen parameters. The difference between experimental and theoretical results with ν = 0 is within the tolerance of the error bar. Therefore, the theoretical results with $\nu = 0$ are in good agreement with the experiment, which implies that the SU-8 film probably does not experience an efficient in-plane deformations transverse to the applied strain

direction. The strain induced to the BP through our experimental setup is very close to a pure uniaxial strain. Therefore, the experimental Grüneisen parameters with $\nu = 0$ have been recalculated based on the experimental Raman shift rates and also listed in Table 1. The discrepancy of Grüneisen parameters between the experiment and the calculation is much smaller for $\nu = 0$ than that for $\nu = 0.33$. The recalculated in-plane Grüneisen parameters of the B_{2g} mode ($\gamma_{B_{2g}}$) for the ZZ strain is 2.47. Although it is smaller than the value calculated with $\nu = 0.33$, it is still larger than those of graphene and MoS_2, implying the giant anharmonicity and strain anisotropy in ultrathin BP.

The gaint anisotropic strain-dependent Raman shift rate of the B_{2g} mode has prompted us to utilize this property for identifying the crystal orientation of ultrathin BP. **Figure S6** (Supporting Information) illustrates the specific schematic process of the crystallographic identification method for ultrathin BP. Another flake of ~ 6.8 nm thick BP was prepared to verify the proposed method. A PET substrate with circular shape was used instead of a previously adopted rectangular one. A total of 18 pairs of parallel edges were tailored out along the perimeter of the circular substrate so that the strain can be applied perpendicular to a pair of parallel edges. A fixed value of 0.46% strain was applied to the sample. **Figure 4**a shows an optical image of the new BP sample and rotation direction. The non-polarized Raman spectra was recorded as a function of the sample rotation angle by a step of 10^o. The rotation angle (δ) dependent variations of Raman shifts for the three modes are shown in **Figure 4**b, in which sine-like variations are observed. Notably, the Raman shift variation of the A_g^1 mode is out of phase as compared with the A_g^2 and B_{2g} modes, which is consistent with our previous findings. Moreover, the B_{2g} mode exhibits only red-shift and its variation is much larger than those of the other two modes for about two times. This intriguing property of the B_{2g} mode can be utilized as a pointer to the ZZ and AC orientations according to our experimental results. The ZZ direction of the ultrathin BP can be identified if the variation of Raman shift for the B_{2g} mode arrives to its local maximum as shown in **Figure 4**c where the ZZ direction is marked at $\delta \approx 40°$. Correspondingly, the transverse direction ($\delta \approx 130°$) is the AC direction. In order to verify these results, conventional angle-

resolved polarized Raman spectroscopy was also performed. Indeed, the AC direction is found to be at $\delta \approx 130°$ according to the measured maximum intensity of the A_g^2 mode along this direction as shown in **Figure 4**d. Thus, the ZZ orientation can be determined to be at $\delta \approx 40°$, which is consistent with the results revealed by rotating the strained BP sample. In another control experiment, the Raman spectra of the unstrained sample were measured at δ = 0°, 30° , 60° and 90° in non-polarized Raman configuration as shown in **Figure S7** (Supporting Information). No variations of the Raman shifts for the three modes can be observed. Therefore, by simply monitoring the variation of Raman shift for the B_{2g} mode in ultrathin BP as a function of the applied strain in various angles, the two characteristic orientations of ultrathin BP can be determined easily and precisely.

3. Conclusion

In summary, we comprehensively studied the anisotropic strain response in Raman modes of the ultrathin BP using a modified bending technique. The B_{2g} mode was found to be extremely sensitive to the ZZ strain with the Raman shift rate and the Grüneisen parameter of colossal values of ~ -11 cm^{-1}/% strain and ~2.5 respectively. By comparing with the results calculated by DFT method, the effective Poisson's ratio applied to the BP samples is estimated to be ~0 in the experiment, which enables us to enhance the accuracy of the calculation of Grüneisen parameters. It demonstrates that this bending technique can offer a quasi-pure uniaxial tensile strain to ultrathin BP. Our theoretical calculation suggests that the giant anisotropic strain response in ultrathin BP is ascribed to the changes in both bond lengths and angles of the BP upon applied strain. Based on the giant anisotropic strain response in B_{2g} mode, we demonstrate a facile method to identify the crystallographic orientations of the ultrathin BP using the strained ultrathin BP and the conventional non-polarized Raman spectroscopy. Our work paves a way to explore the anisotropic strain-dependent electrical, optical and thermal properties of ultrathin BP devices.

4. Experimental Section

Fabrication and Characterization of Encapsulated Ultrathin Black Phosphorus: Ultrathin BP were prepared by the modified mechanical exfoliation from bulk BP single crystals (from Smart-Elements) using Polydimethylsiloxane (PDMS) film (from Gel-Pak).[43] Then, the ultrathin BP was deposited onto a 121 μm thick clear flexible PET substrate with an area of 24 mm × 20 mm. Before the deposition, a layer of SU-8 photoresist (~400 nm) was pre-coated on the PET substrate for enhancing the visibility of ultrathin BP and reducing the surface roughness of the substrate, which can ensure a good adhesion of the ultrathin BP on the PET.[35, 44] The mechanically exfoliated ultrathin BP was deposited at the center of the PET as far as possible. As the size of the ultrathin BP is much smaller than the thickness of PET, the induced strain to the flakes can be assumed to be the same as the applied strain to the PET substrate.[38] Finally, the deposited ultrathin BP was immediately covered by a thin layer (~100 nm) of polymethyl methacrylate (PMMA) which could prevent the slippage and protect the ultrathin BP from degradation in the ambient. The residual BP on the PDMS film was transferred onto the copper grid for TEM measurement. TEM analysis was carried out using an ultrahigh resolution (0.1 nm) transmission electron microscope (JEOL JEM-2100F) operated with an acceleration voltage of 200 kV. AFM (Veeco Multimode 8) was carried out finally to determine the thickness of the ultrathin BP in tapping mode.

Raman Spectrum Measurement: All the Raman spectroscopy measurements were conducted on Horiba HR800 Raman spectroscopy system. An external liner polarized diode pumped solid state laser of 488 nm was utilized to excite the samples in the confocal Raman system. We used a 100 × objective lens to focus the laser onto the sample with a spot size of ~ 1.0 μm. The diffraction grating was set as 1800 Grooves/mm. The resolution of the confocal Raman system can reach 0.6 cm^{-1}. The power of incident laser on the sample is attenuated to 15 μW to prevent the degradation of the ultrathin BP and reduce sample heating. For angle-resolved polarized Raman measurement, a half wave plate was inset into the path of incident laser to tune the polarization direction. An analyzer was placed into the path of scattered light and set as parallel to the initial polarization direction of incident laser.

Another quarter wave plate fixed at 45^{o} was placed between the analyzer and the detector to minimize the error resulted from the spectrometer itself.

Aligning Specific Strain Directions: A polar coordinate paper with resolution of 10^{o} was utilized so that the strain can be applied to a specified direction. A clear transparent PET substrate was fixed on the coordinate paper and then a pair of parallel edges of the PET substrate was cut out where the edges are perpendicular to the applied strain direction. In the process of clipping specific edges of the PET substrate, the position of our BP sample was almost kept at the center of the PET substrate.

First Principle Calculations: Density functional theory calculations were performed using the generalized gradient approximation for the exchange-correlation potential, the projector augmented wave method[45, 46] and a plane-wave basis set as implemented in the Vienna ab-initio simulation package (VASP)[47]. Vibrational properties were calculated using Density functional perturbation theory.[48] The vdW-DF method[49, 50] was used to describe the van der Waals interactions together with the optB86b exchange function,[51, 52] which is proved to be accurate in reproducing the atomic structure of layered materials.[5, 53, 54] The unit cell contained 4 layers of BP with 20Å vacuum slab. Energy cut-off for plane-wave basis was set to 700 eV throughout the calculation. A 31×31×1 k-mesh was used to sample the first Brillouin zone of unit cell. Strain was introduced by modifying lattice parameters, and all atoms were fully relaxed until the residual force was less than 0.0001 eV/Å. Calculated vibrational frequencies were rescaled by a uniform scaling factor of 1.0612 to make better comparison with experimental results, which is a regular procedure.[55]

Supporting Information

Supporting Information is available from the Wiley Online Library or from the author.

Acknowledgements

This work was financially supported by the PolyU grants (1-ZE14 and 1-ZVGH) and the Research Grants Council (RGC) of Hong Kong (Project no. PolyU 153030/15P). One of the authors (SHL)

acknowledges the support from the Postdoctoral Science Foundation of China (No. 7131701013), Hong Kong Scholars Program (No. G-YZ36).

[1] K. S. Novoselov, A. K. Geim, S. V. Morozov, D. Jiang, Y. Zhang, S. V. Dubonos, I. V. Grigorieva, A. A. Firsov, *Science* **2004**, 306, 666.

[2] A. Splendiani, L. Sun, Y. Zhang, T. Li, J. Kim, C. Y. Chim, G. Galli, F. Wang, *Nano Lett.* **2010**, 10, 1271.

[3] A. Loiseau, F. Willaime, N. Demoncy, G. Hug, H. Pascard, *Phys. Rev. Lett.* **1996**, 76, 4737.

[4] Y. Akahama, S. Endo, S. i. Narita, *J. Phys. Soc. Jpn* **1983**, 52, 2148.

[5] J. Qiao, X. Kong, Z. X. Hu, F. Yang, W. Ji, *Nat. Commun.* **2014**, 5, 4475.

[6] L. Li, Y. Yu, G. J. Ye, Q. Ge, X. Ou, H. Wu, D. Feng, X. H. Chen, Y. Zhang, *Nat. Nanotechnol.* **2014**, 9, 372.

[7] F. Xia, H. Wang, Y. Jia, *Nat. Commun.* **2014**, 5, 4458.

[8] Z. Luo, J. Maassen, Y. Deng, Y. Du, R. P. Garrelts, M. S. Lundstrom, P. D. Ye, X. Xu, *Nat. Commun.* **2015**, 6, 8572.

[9] R. Fei, L. Yang, *Nano Lett.* **2014**, 14, 2884.

[10] Z. Y. Ong, Y. Cai, G. Zhang, Y. W. Zhang, *J. Phys. Chem. C* **2014**, 118, 25272.

[11] Y. Li, S. Yang, J. Li, *J. Phys. Chem. C* **2014**, 118, 23970.

[12] R. Fei, L. Yang, *Appl. Phys. Lett.* **2014**, 105, 083120.

[13] A. S. Rodin, A. Carvalho, A. H. Castro Neto, *Phys. Rev. Lett.* **2014**, 112, 176801.

[14] V. Pereira, A. Castro Neto, N. Peres, *Phys. Rev. B* **2009**, 80.

[15] Y. Y. Hui, X. Liu, W. Jie, N. Y. Chan, J. Hao, Y. T. Hsu, L. J. Li, W. Guo, S. P. Lau, *ACS Nano* **2013**, 7, 7126.

[16] Y. Kato, R. C. Myers, A. C. Gossard, D. D. Awschalom, *Nature* **2004**, 427, 50.

[17] X. Peng, Q. Wei, A. Copple, *Phys. Rev. B* **2014**, 90, 085402.

[18] J. S. Kim, Y. Liu, W. Zhu, S. Kim, D. Wu, L. Tao, A. Dodabalapur, K. Lai, D. Akinwande, *Sci. Rep.* **2015**, 5, 8989.

[19] S. P. Koenig, R. A. Doganov, H. Schmidt, A. H. Castro Neto, B. Özyilmaz, *Appl. Phys. Lett.* **2014**, 104, 103106.

[20] J. Pei, X. Gai, J. Yang, X. Wang, Z. Yu, D. Y. Choi, B. Luther Davies, Y. Lu, *Nat. Commun.* **2016**, 7, 10450.

[21] Y. Wang, C. Cong, R. Fei, W. Yang, Y. Chen, B. Cao, L. Yang, T. Yu, *Nano Research* **2015**, 8, 3944.

[22] J. Wu, N. Mao, L. Xie, H. Xu, J. Zhang, *Angew. Chem. Int. Ed.* **2015**, 127, 2396.

[23] W. Lu, X. Ma, Z. Fei, J. Zhou, Z. Zhang, C. Jin, Z. Zhang, *Appl. Phys. Lett.* **2015**, 107, 021906.

[24] H. B. Ribeiro, M. A. Pimenta, C. J. S. d. Matos, R. L. Moreira, A. S. Rodin, J. D. Zapata, E. z. A. T. d. Souza, A. H. C. Neto, *ACS Nano* **2015**, 9, 4270.

[25] Y. Akahama, M. Kobayashi, H. Kawamura, *Solid State Commun.* **1997**, 104, 311.

[26] H. J. Conley, B. Wang, J. I. Ziegler, R. F. Haglund, Jr., S. T. Pantelides, K. I. Bolotin, *Nano Lett.* **2013**, 13, 3626.

[27] H. Liu, A. T. Neal, Z. Zhu, Z. Luo, X. Xu, D. Tománek, P. D. Ye, *ACS Nano* **2014**, 8, 4033.

[28] S. Lin, S. Liu, Z. Yang, Y. Li, T. W. Ng, Z. Xu, Q. Bao, J. Hao, C. S. Lee, C. Surya, F. Yan, S. P. Lau, *Adv. Func. Mater.* **2016**, 26, 864.

[29] H. O. Churchill, P. Jarillo Herrero, *Nat. Nanotechnol.* **2014**, 9, 330.

[30] X. Wang, A. M. Jones, K. L. Seyler, V. Tran, Y. Jia, H. Zhao, H. Wang, L. Yang, X. Xu, F. Xia, *Nat. Nanotechnol.* **2015**, 10, 517.

[31] X. Ling, L. Liang, S. Huang, A. A. Puretzky, D. B. Geohegan, B. G. Sumpter, J. Kong, V. Meunier, M. S. Dresselhaus, *Nano Lett.* **2015**, 15, 4080.

[32] J. Kim, J. U. Lee, J. Lee, H. J. Park, Z. Lee, C. Lee, H. Cheong, *Nanoscale* **2015**, 7, 18708.

[33] X. Ling, S. Huang, E. H. Hasdeo, L. Liang, W. M. Parkin, Y. Tatsumi, A. R. Nugraha, A. A. Puretzky, P. M. Das, B. G. Sumpter, D. B. Geohegan, J. Kong, R. Saito, M. Drndic, V. Meunier, M. S. Dresselhaus, *Nano Lett* **2016**, 16, 2260.

[34] D. Yoon, Y. W. Son, H. Cheong, *Phys. Rev. Lett.* **2011**, 106, 155502.

[35] G. Tsoukleri, J. Parthenios, K. Papagelis, R. Jalil, A. C. Ferrari, A. K. Geim, K. S. Novoselov, C. Galiotis, *Small* **2009**, 5, 2397.

[36] T. Mohiuddin, A. Lombardo, R. Nair, A. Bonetti, G. Savini, R. Jalil, N. Bonini, D. Basko, C. Galiotis, N. Marzari, K. Novoselov, A. Geim, A. Ferrari, *Phys. Rev. B* **2009**, 79, 205433.

[37] Y. Wang, C. Cong, C. Qiu, T. Yu, *Small* **2013**, 9, 2857.

[38] C. Rice, R. J. Young, R. Zan, U. Bangert, D. Wolverson, T. Georgiou, R. Jalil, K. S. Novoselov, *Phys. Rev. B* **2013**, 87, 081307(R).

[39] S. Sugai, T. Ueda, K. Murase, *J. Phys. Soc. Jpn* **1981**, 50, 3356.

[40] Z. X. Hu, X. Kong, J. Qiao, B. Normand, W. Ji, *Nanoscale* **2016**, 8, 2740.

[41] G. Grimvall, *Thermophysical Properties of Materials*, Elsevier, Amsterdam, North Holland, Netherlands 1999.

[42] J. Zabel, R. R. Nair, A. Ott, T. Georgiou, A. K. Geim, K. S. Novoselov, C. Casiraghi, *Nano Lett.* **2012**, 12, 617.

[43] A. Castellanos Gomez, M. Buscema, R. Molenaar, V. Singh, L. Janssen, H. S. J. van der Zant, G. A. Steele, *2D Materials* **2014**, 1, 011002.

[44] C. Casiraghi, A. Hartschuh, E. Lidorikis, H. Qian, H. Harutyunyan, T. Gokus, K. S. Novoselov, A. C. Ferrari, *Nano Lett.* **2007**, 7, 2711.

[45] P. E. Blöchl, *Phys. Rev. B* **1994**, 50, 17953.

[46] G. Kresse, D. Joubert, *Phys. Rev. B* **1999**, 59, 1758.

[47] G. Kresse, J. Furthmüller, *Phys. Rev. B* **1996**, 54, 11169.

[48] S. Baroni, S. de Gironcoli, A. Dal Corso, P. Giannozzi, *Rev. Mod. Phys.* **2001**, 73, 515.

[49] M. Dion, H. Rydberg, E. Schröder, D. C. Langreth, B. I. Lundqvist, *Phys. Rev. Lett.* **2004**, 92, 246401.

[50] K. Lee, É. D. Murray, L. Kong, B. I. Lundqvist, D. C. Langreth, *Phys. Rev. B* **2010**, 82, 081101.

[51] K. Jiří, R. B. David, M. Angelos, *J. Phys.: Condens. Matter* **2010**, 22, 022201.

[52] J. Klimeš, D. R. Bowler, A. Michaelides, *Phys. Rev. B* **2011**, 83, 195131.

[53] J. B. Wu, Z. X. Hu, X. Zhang, W. P. Han, Y. Lu, W. Shi, X. F. Qiao, M. Ijiäs, S. Milana, W. Ji, A. C. Ferrari, P. H. Tan, *ACS Nano* **2015**, 9, 7440.

[54] J. Hong, Z. Hu, M. Probert, K. Li, D. Lv, X. Yang, L. Gu, N. Mao, Q. Feng, L. Xie, J. Zhang, D. Wu, Z. Zhang, C. Jin, W. Ji, X. Zhang, J. Yuan, Z. Zhang, *Nat. Commun.* **2015**, 6, 7293.

[55] A. P. Scott, L. Radom, *J. Phys. Chem.* **1996**, 100, 16502.

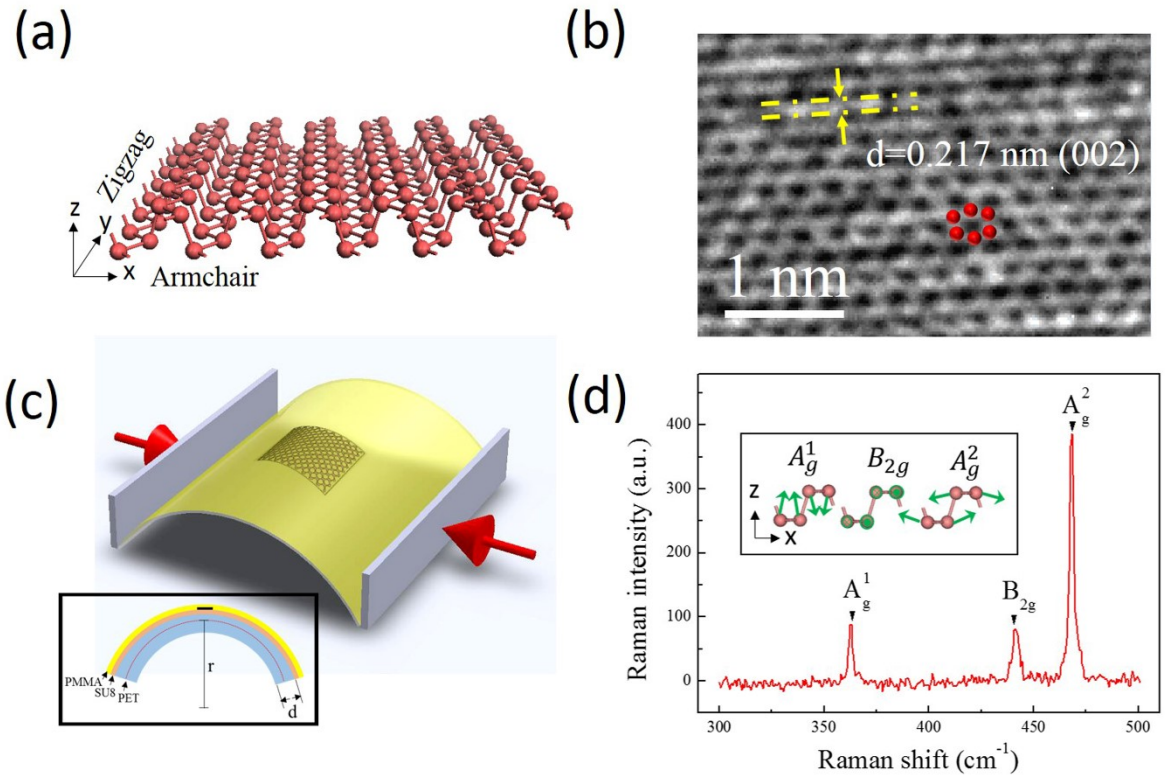

Figure 1. (a) Atomic lattice structure of a monolayer BP. Wrinkled layer can be observed clearly. (b) High-resolution TEM image of the ultrathin BP. The (002) crystal spacing is marked. Hexagonal atomic structure is illustrated by red balls. (c) Schematic diagram (not to scale) of the experimental setup. Two point bending method is utilized to supply tunable uniaxial strain along specific directions. The inset shows the cross-sectioned profile of the polymer encapsulated ultrathin BP. The ultrathin BP is sandwiched by the bottom SU-8 photoresist layer and the top PMMA layer. (d) Raman spectrum of the encapsulated ultrathin BP on PET substrate without applied uniaxial strain. Inset: the corresponding atomic displacement for the three Raman modes.

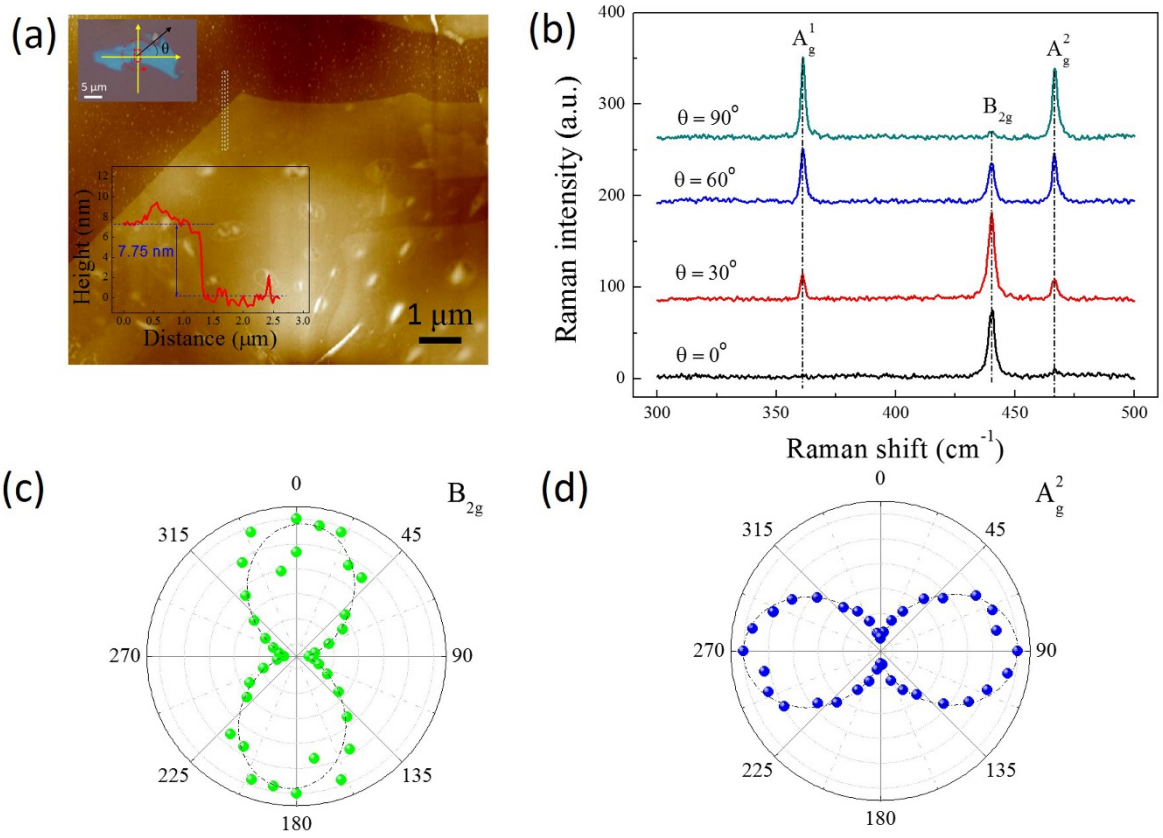

Figure 2. (a) AFM image of the ultrathin BP after removing the protective PMMA layer. The bottom insert is the AFM height profile of the BP revealing the thickness of ~7.75 nm. The top inset shows the optical image of the BP sample on the PET substrate. θ is the polarization axis of the incident laser which can be tuned by a half-wave plate. (b) Polarized Raman spectra of the encapsulated BP with different polarization angles. (c-d) Polar plots of the polarized Raman peak intensities of B_{2g} and A_g^2 modes, respectively. Fittings are represented by black dash dot lines.

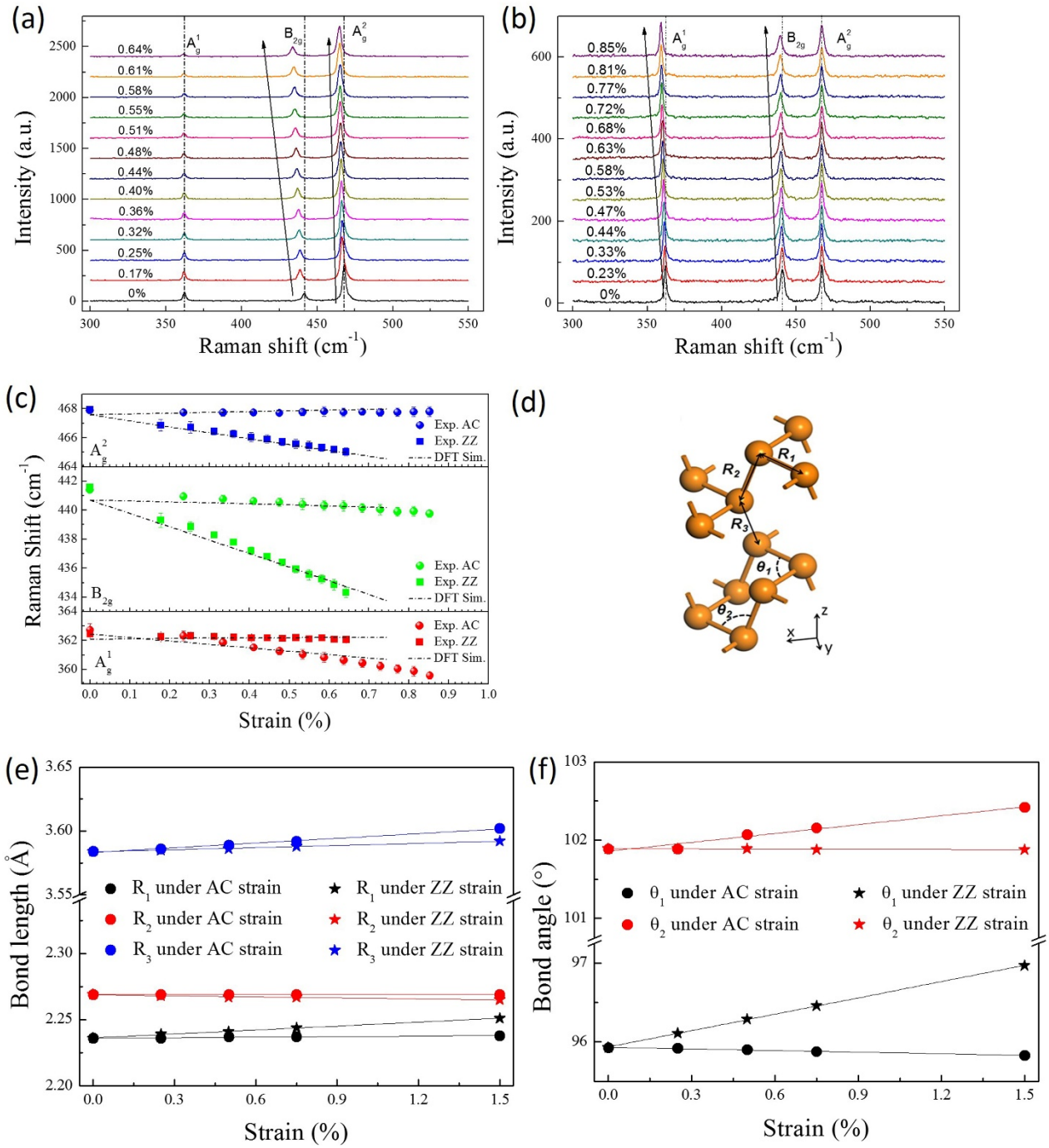

Figure 3. Evolution of the Raman spectra of A_g^1, B_{2g} and A_g^2 modes of the encapsulated ultrathin BP on PET substrate under the uniaxial strain along zigzag direction (a) and armchair direction (b). The black arrow lines are the guides of the peak centers. (c) Raman shifts of A_g^1, B_{2g} and A_g^2 modes as a function of the applied strain along ZZ and AC directions. The Raman system is in non-polarized configuration during the measurement. The dash dot lines are simulated results based on the DFT

calculations, in which the in-plane Poisson's ratio is set as zero ($\nu = 0$). (d) The 3-dimensional view of BP structure giving the definitions of structural parameters. R_1 and R_2 are two kinds of P-P bond lengths. θ_1 and θ_2 are the bonding angles. R_3 is the nearest distance between interlayer atoms. (e) DFT calculated bond lengths R_1, R_2 and R_3 as a function of uniaxial tensile strain along ZZ and AC directions. (f) DFT calculated bond angles θ_1 and θ_2 as a function of uniaxial strain along the ZZ and AC directions.

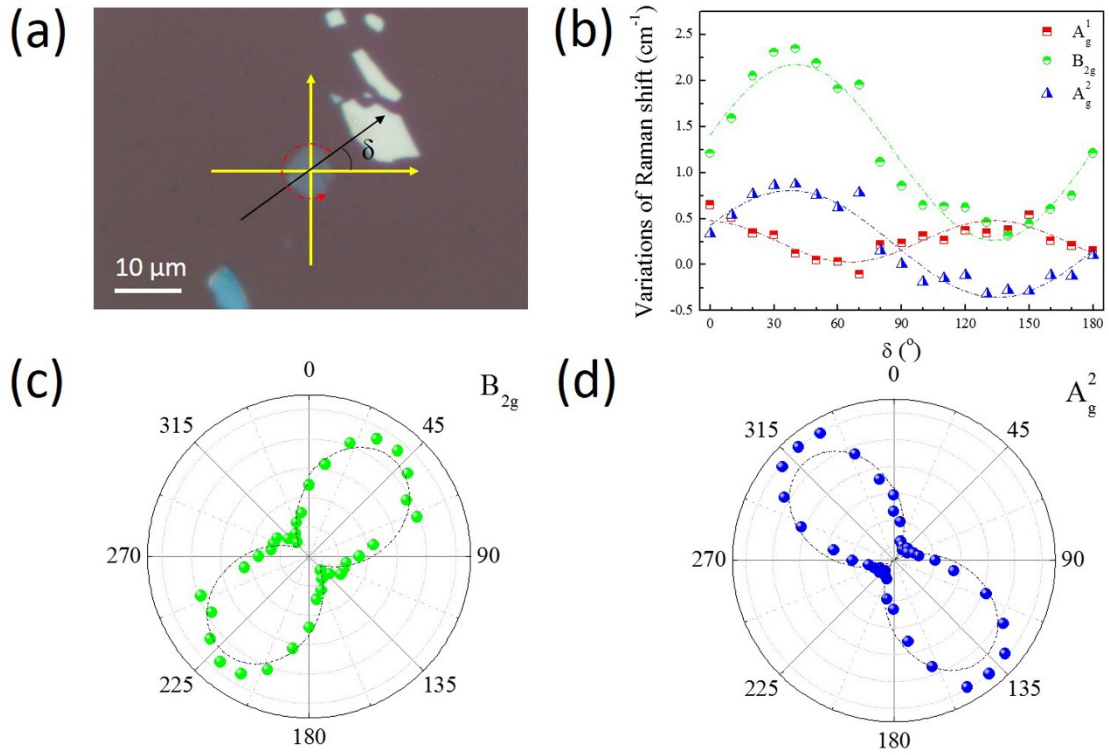

Figure 4. (a) Optical image of another encapsulated ultrathin BP flakes. The coordinate system employed in this experiment is shown. The direction (δ) of the strained sample is rotated in-plane along the direction illustrated by the red dashed arrow. (b) The variations of Raman shifts as a function of the applied strain direction for A_g^1, B_{2g} and A_g^2 modes of the ultrathin BP are presented. A constant uniaxial tensile strain of 0.46% is applied. The Raman system is in non-polarized configuration. (c) Polar plot of the variation of Raman shift for B_{2g} mode as a function of δ. The Raman shift of B_{2g} mode arrives at maximum at ~ 40° meaning that this direction is the ZZ orientation. (d) Polar plot of the conventional angle-resolved polarized Raman intensity of A_g^2 mode as a control experiment. The maximum intensity occurs at ~ 130° indeed demonstrating this direction as AC direction and a corresponding transverse direction is the ZZ direction.

Table 1. Raman shift rates (defined by $\partial\omega/\partial\varepsilon$, $cm^{-1}/\%$ strain) of the three characteristic Raman modes and the dimensionless anisotropic Grüneisen parameters (γ) in the ultrathin BP under the ZZ and AC directional strain. Both cases with Poisson's ratio equals to 0 and 0.33 are considered and listed here. The subscripts (Exp.) and (Sim.) represent the values obatined from experiment and DFT calculation respectively.

Strain direction	Ramam mode	$\partial\omega/\partial\varepsilon_{(\text{Exp.})}$	$\partial\omega/\partial\varepsilon_{(\text{Sim.})}$ $(\nu=0)$	$\partial\omega/\partial\varepsilon_{(\text{Sim.})}$ $(\nu=0.33)$	$\gamma_{(\text{Exp.})}$ $(\nu=0)$	$\gamma_{(Sim.)}$ $(\nu=0)$	$\gamma_{(\text{Exp.})}$ $(\nu=0.33)$	$\gamma_{(Sim.)}$ $(\nu=0.33)$
Zigzag	A_g^1	-0.52±0.06	0.19	1.12	0.14	-0.05	0.22	-0.45
	B_{2g}	10.92±0.22	-9.27	-9.11	2.47	2.10	3.69	3.09
	A_g^2	-4.32±0.11	-4.06	-4.10	0.92	0.87	1.38	1.31
Armchair	A_g^1	-3.81±0.15	-2.35	-2.21	1.05	0.63	1.57	0.89
	B_{2g}	-1.85±0.05	-0.70	2.16	0.42	0.16	0.63	-0.73
	A_g^2	-0.03±0.05	0.52	2.01	0.01	-0.11	0.01	-0.64

Table 2. The slopes of the DFT calculated representative structural parameters based on a 4L-BP model under the ZZ and AC uniaxial strain.

Strain direction	R_1 [Å/% strain]	R_2 [Å/% strain]	R_3 [Å/% strain]	θ_1 [°/% strain]	θ_2 [°/% strain]
Zigzag	0.010	-0.003	0.003	0.627	-0.007
Armchair	0.001	0.000	0.012	-0.067	0.353

The table of contents

Giant anisotropic Raman response in ultrathin black phosphorus has been investigated by a modified bending technique. We demonstrate the Raman shift rate and Grüneisen parameter of the B_{2g} mode can reach colossal values of ~-11 cm^{-1}/% strain and ~2.5 respectively under uniaxial strain applied along zigzag direction.

Keywords: black phosphorus, uniaxial strain, Raman spectroscopy, Grüneisen parameter, anisotropy

Yanyong Li, Zhixin Hu, Shenghuang Lin, Sin Ki Lai, and Wei Ji*, Shu Ping Lau*

Giant Anisotropic Raman Response of Encapsulated Ultrathin Black Phosphorus by Uniaxial Strain